Experimental Techniques
https://doi.org/10.1007/s40799-023-00682-w

RESEARCH PAPER

Experimental Modal Analysis and Operational Deflection Shape Analysis of a Cantilever Plate in a Wind Tunnel with Finite Element Model Verification

D. T. Will[1] · W. D. Zhu[1]

Received: 13 February 2023 / Accepted: 15 September 2023

Abstract
This work explores the response of a cantilever plate attached to a cylinder in a wind tunnel under an impact excitation. A detailed computer-aided design (CAD) model and the finite element analysis (FEA) modal simulation of the experimental setup are introduced. Two experimental techniques are thoroughly discussed: an accelerometer-based experimental modal analysis (EMA) method, and a non-contact, full-field, high-speed digital image correlation (DIC)-based operational deflection shape (ODS) analysis method. The experimental and FEA results of the first seven natural frequencies, mode shapes, and ODSs of the cantilever plate are presented and compared. The percent differences between the EMA and FEA natural frequency results are less than 4.8%, and the modal assurance criterion (MAC) values between the EMA and FEA mode shapes are at least 0.845. The percent differences between the ODS analysis and FEA natural frequency results are less than 3.4%, while the MAC values between the ODS analysis ODSs and FEA mode shapes are at least 0.728. The percent differences between the EMA and ODS analysis natural frequency results are less than 3.5%, and the MAC values between the EMA mode shapes and ODS analysis ODSs are at least 0.505. There are two sets of two different mode shapes and ODSs with relatively high correlation. One set is a set of two closely spaced modes and ODSs approximately 20 Hz apart with obvious similarities in shape. The other set is a set of two modes and ODSs approximately 100 Hz apart that share less obvious similarities in shape.

Keywords Experimental modal analysis · Operational deflection shape analysis · Finite element analysis · Cantilever plate · Wind tunnel · Digital image correlation

Introduction

Cantilever plates, or flexible splitter plates, have been proposed for use as passive noise-reduction and vibration suppression devices in aerodynamic and hydrodynamic flow fields, as they act to disrupt the natural vortex shedding that occurs behind bluff bodies immersed in flow fields [1–3]. Flexible splitter plates have also been used to model biological applications such as a soft palate vibrating within the pharynx of a human airway, which is known to cause snoring and sleep apnea [4]. Other applications include energy harvesting [5] and flexible membrane wings for greater aerodynamic efficiency in micro-air-vehicle flight [6]. These diverse fluid–structure interaction (FSI) applications inspire the need to study various measurement and analysis techniques for cantilever plate vibration.

In the analysis of vibration of rectangular plates, it is well known that the differential equation describing the motion of a plate cannot be solved directly for most boundary condition cases [7, 8]. To overcome this issue, several approaches to solving for approximate solutions of rectangular cantilever plates have been developed, including variational methods, such as the Rayleigh–Ritz method, Galerkin's method, and Vlasov's method, and finite element methods [9]. Warburton [10] used the Rayleigh–Ritz method to calculate frequency equation coefficients for every combination of boundary conditions of a rectangular plate. This allows for

D. T. Will and W. D. Zhu are members of SEM.

✉ W. D. Zhu
wzhu@umbc.edu

D. T. Will
dwill1@umbc.edu

[1] Department of Mechanical Engineering, University of Maryland, Baltimore County, 1000 Hilltop Circle, Baltimore, MD 21250, USA

Published online: 20 November 2023

an approximation of natural frequencies and subsequent prediction of the displacement at any point on the plate under free vibration. Leissa [11] compiled a survey of literature on analytical and numerical solutions for vibrations of plates, including circular, rectangular, and anisotropic plates, and plates of variable thicknesses. With modern computers, analysis is usually performed with finite element methods using commercially available software such as Nastran, ANSYS, and Abaqus.

Experimental methods are used across all engineering domains to study a system's response to some specified input or forcing function. Methods of EMA have evolved from contact-based impact hammer [12] or shaker excitation [13] and accelerometer response measurement [14], to non-contact speaker excitation [15] and laser vibrometer [16], photogrammetry [17], or DIC response measurement [15], to any combination of these excitation and response measurement techniques. Gülbahçe and Çelik [18] developed a roving shaker, fixed accelerometer approach to plate excitation and response measurement, respectively, and found that this approach had higher correlation to FEA results than the roving hammer technique. Improvements in modal parameter estimation have also been made, with the PolyMAX algorithm [19] developed by LMS International, now acquired by Siemens, considered to be a high-performance algorithm in terms of producing clear stabilization diagrams, accurate results, and computational efficiency [18]. Whalen et al. [20] used non-contact photogrammetry to investigate FSI between hypersonic flow and a plate clamped on all sides. Among other interesting findings, researchers noted mode shapes correlated well with expected results from the classical plate theory, but natural frequencies shifted with changes in the shock-wave/boundary-layer interaction intensity due to subsequent temperature changes in the plate. As the cost of high-speed cameras continues to decrease, more DIC-based ODS analysis research becomes available. Yu and Pan developed a lower-cost DIC technique that used a single high-speed camera with four mirrors for viewing a test object via two separate optical paths [21], and they successfully demonstrated the single-camera DIC technique on a rotating structure [22]. Xie et al. [23] studied the vibration of a flexible splitter plate behind a cylinder in a wind tunnel using a single-camera high-speed stereo-DIC system. Warren et al. [12] compared frequency response functions (FRFs) of a cantilever plate captured using DIC, three-dimensional (3D) point tracking, 3D laser vibrometer, and accelerometer measurements. Results showed high correlation to an FEA-based modal analysis. Witt and Rohe [24] explored the use of DIC as a modal analysis technique, showing that FRFs may be generated by combining the DIC displacement data with the excitation force data measured with an independent data acquisition system. The collected input and response signals are then time-synced in post-processing to compute the FRFs. More recently, Frankovský et al. [25] developed an application module for DIC that generates FRFs of a structure using excitation data from an impact hammer and response data collected from high-speed cameras. This application module allowed for estimation of modal parameters of the structure, such as natural frequencies, damping coefficients, and mode shapes. Jones and Iadicola (Eds.) [26] of the International Digital Image Correlation Society have published a DIC good practices guide which aims to standardize DIC testing procedures and reporting requirements across the DIC community. The guide contains detailed information on design, setup, execution, post-processing, and reporting information for DIC experiments and research.

This paper provides a detailed design and experimental setup for the FEA, EMA, and ODS analysis of a cantilever plate attached to a cylinder in a wind tunnel. A novel cylinder design is introduced which allows for clamping of the cantilever plate, while also ensuring there is no gap between the two half-cylinders. The design of an experimental test structure will be introduced, including its CAD model, finite element model (FEM), and FEA simulation setup. Then, the EMA experimental setup and testing in the wind tunnel are discussed, followed by the ODS analysis experimental setup and testing. Next, the EMA and FEA results and their analyses are presented, followed by the ODS analysis and FEA results and their analyses, and subsequently, the EMA and ODS analysis results and their analyses. Finally, a discussion on the presence of a 577.042 Hz in-plane mode shape in the FEA results that was not observable in the EMA or ODS analysis is presented. This paper aims to establish a connection between the EMA and ODS analysis, including a novel approach for comparing the mode shapes, captured using the EMA or FEA, with ODSs, captured using the Correlated Solutions, Inc. high-speed DIC system. This paper serves as a precursor to future research in FSI of a cantilever plate immersed in air flow inside a wind tunnel.

Methods

Design, Modeling, and Simulation

The design for the experimental setup was developed using Siemens NX CAD software, given size constraints for the experiment in an AEROLAB Educational Wind Tunnel whose test section was 304.8 mm wide and 304.8 mm tall, and whose length was 609.6 mm long. Mounting provisions inside the test section were limited, the surrounding structure was not perfectly rigid, and the boundary conditions in the wind tunnel were imperfect. A 152.4 mm tall, 152.4 mm wide, and 2.54 mm thick aluminum 2024-T3 cantilever plate clamped between two 6061-T6 half-cylinders with a diameter of 31.8 mm was modeled. The two half-cylinders were

each slotted at a depth of 1.27 mm, or half the thickness of the cantilever plate, to allow the two half-cylinders to be flush against each other while clamping the cantilever plate, as shown in Fig. 1. This design ensured the cantilever plate was clamped, while also ensuring that there was no gap between the two half-cylinders for uninterrupted air flow over the cylinder in future FSI research. One half-cylinder was threaded, and the other half-cylinder had counterbored thru-holes to allow 300-series stainless steel fasteners to pass through the plate and provide clamping forces to the plate. After assembly, the exposed plate surface was 152.4 mm tall and 128.6 mm wide. Upper and lower brackets were modeled to securely fasten the cylinder to the test section. At the lower boundary condition, an aluminum 6061-T6 rectangular bracket, 12.7 mm tall, 43.3 mm wide, and 93.0 mm long, with counterbored thru-holes allowed for fastening the two half-cylinders to the bracket with 300-series stainless steel fasteners, which was then fastened to the base of the test section with 300-series stainless steel fasteners. At the upper boundary condition, a 38.1 mm tall, 38.1 mm wide, and 596.9 mm long aluminum 6061-T6 angle bracket with thru-holes and slots allowed for fastening the two half-cylinders to the bracket with 300-series stainless steel fasteners, which was then fastened to the top of the test section with 300-series stainless steel fasteners. For the FEA that modeled the EMA case, the accelerometer and accelerometer wire masses were not modeled because it was found to be difficult to accurately determine the effective mass loading of the accelerometer wire on the cantilever plate. For the FEA that modeled the ODS analysis case, no accelerometer and accelerometer wire masses were modeled because they were not present in the ODS analysis. The CAD model of the experimental setup with dimensions is shown in Fig. 2.

An FEA-based modal analysis of the experimental setup was performed to model the structure using the Siemens NX Pre/Post application FEA software. A 3D tetrahedral ("tet") mesh was generated for each individual FEM part, including

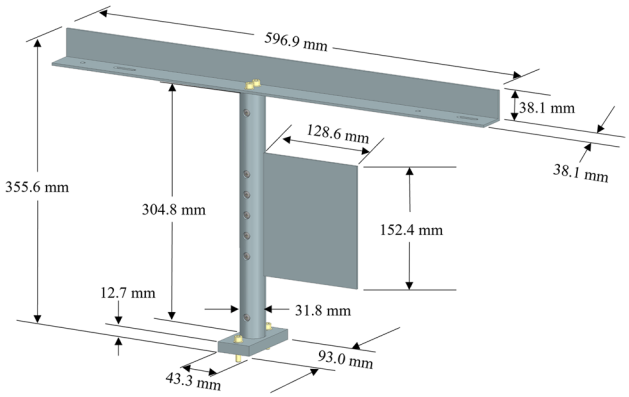

Fig. 2 The CAD model of the experimental setup that includes the cantilever plate, two half-cylinders, upper- and lower-cylinder mounting brackets, and fastening hardware

the cantilever plate, two half-cylinders, and the upper- and lower-cylinder mounting brackets. An FEA convergence study on the tetrahedral mesh element size was performed to show convergence of the natural frequency results with decreasing mesh element size. The natural frequency results from the different mesh element sizes are compared with a percent difference calculation given by

$$\text{Percent Difference } (\%) = \frac{|a-b|}{[(a+b)/2]} \times 100 \tag{1}$$

where a is the natural frequency in the first dataset and b is the corresponding natural frequency in the second dataset. Mesh element sizes of 7.62 mm, 2.54 mm, and 1.27 mm were tested, and there were natural frequency percent differences of less than 0.71% between mesh element sizes of 7.62 mm and 2.54 mm and natural frequency percent differences of less than 0.34% between mesh element sizes of 2.54 mm and 1.27 mm, as shown in Tables 1 and 2, respectively. Note that mode 4* is an in-plane mode shape only, with no

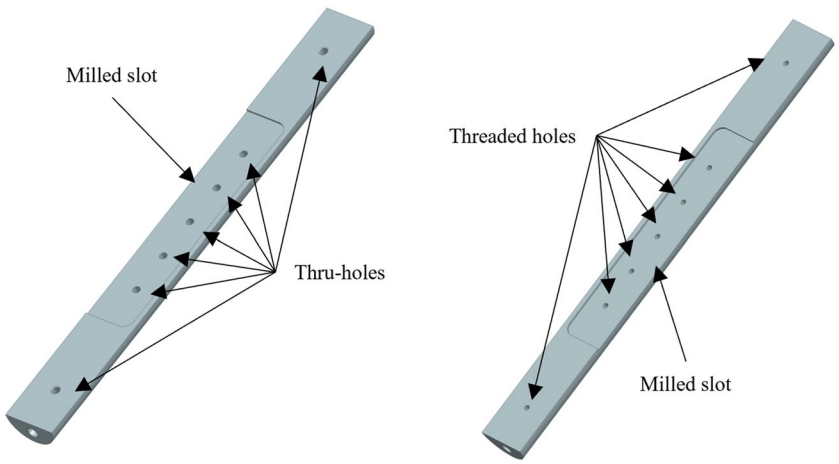

Fig. 1 The CAD model of the two half-cylinders with milled slots to allow for clamping of the cantilever plate while ensuring that there was no gap between the two half-cylinders when assembled

out-of-plane vibration. This mode 4* was not observable using the EMA or ODS analysis techniques in this research. As such, this mode was excluded from the analyses comparing each technique.

After computing the results using a tetrahedral mesh with an element size of 1.27 mm on all components, an FEA simulation was run in which the cantilever plate was meshed with a hexahedral ("hex") mesh with an element size of 1.27 mm. The two half-cylinders, and the upper- and lower-cylinder mounting brackets were meshed with tetrahedral meshes with an element size of 1.27 mm. The resulting natural frequency percent differences were all less than 0.21%, as shown in Table 3.

As the percent differences in the natural frequencies resulting from the cantilever plate being meshed with a hexahedral mesh versus a tetrahedral mesh were minimal at less than 0.21% difference, a 3D tetrahedral mesh with a 1.27 mm element edge length was used for each individual

Table 1 The FEA convergence study results, comparing tetrahedral mesh element sizes of 7.62 mm and 2.54 mm, where all percent differences between the natural frequencies were less than 0.71%

Mode	Natural Frequency (Hz), 7.62 mm Tet Element Size	Natural Frequency (Hz), 2.54 mm Tet Element Size	Percent Difference (%)
1	119.42	118.72	0.588
2	271.32	269.74	0.584
3	289.09	287.07	0.701
4* (In-Plane Mode Shape)	579.19	577.46	0.299
4	626.41	622.48	0.629
5	710.62	706.67	0.557
6	795.86	792.12	0.471
7	1040	1035	0.482

Table 2 The FEA convergence study results, comparing mesh element sizes of 2.54 mm and 1.27 mm, where all percent differences between the natural frequencies were less than 0.34%

Mode	Natural Frequency (Hz), 2.54 mm Tet Element Size	Natural Frequency (Hz), 1.27 mm Tet Element Size	Percent Difference (%)
1	118.72	118.324	0.334
2	269.74	269.149	0.219
3	287.07	286.491	0.202
4* (In-Plane Mode Shape)	577.46	577.042	0.073
4	622.48	620.956	0.245
5	706.67	705.246	0.202
6	792.12	790.987	0.143
7	1035	1032.082	0.282

Table 3 The FEA natural frequency percent differences, comparing the results of tetrahedral mesh element sizes of 1.27 mm on all components with the results of a hexahedral mesh with an element size of 1.27 mm on the cantilever plate and tetrahedral meshes with element sizes of 1.27 mm on all other components. All percent differences between the natural frequencies were less than 0.21%

Mode	Natural Frequency (Hz), 1.27 mm Tet Element Size on All Components	Natural Frequency (Hz), 1.27 mm Hex Element Size on Cantilever Plate, 1.27 mm Tet Element Size on All Other Components	Percent Difference (%)
1	118.324	118.57	0.208
2	269.149	269.50	0.130
3	286.491	286.80	0.108
4* (In-Plane Mode Shape)	577.042	577.45	0.071
4	620.956	621.49	0.086
5	705.246	705.91	0.094
6	790.987	791.49	0.064
7	1032.082	1034	0.186

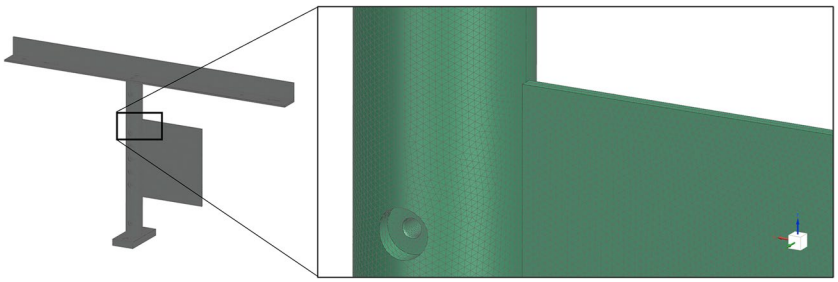

Fig. 3 A view of the FEM meshing with a close-up inset view showing the tetrahedral meshing with 1.27 mm element edge length

Table 4 The FEM material properties for the material used in the FEA model modal analysis

Property	Al 6061-T6	Al 2024-T3
Mass Density	2714.47 kg/m^3	2789.28 kg/m^3
Young's Modulus	68.2581 GPa	72.3949 GPa
Poisson's Ratio	0.33	0.33

FEM part in this work, including the cantilever plate, two half-cylinders, and the upper- and lower-cylinder mounting brackets, as shown in Fig. 3. The FEM material properties for the materials used in the FEA model modal analysis are shown in Table 4. Mesh mating was performed between one surface of the cantilever plate and the corresponding surface of one of the half-cylinders, and then between the opposite surface of the cantilever plate and the corresponding surface of the other half-cylinder.

The fasteners were modeled using RBE2 elements and zero-length CBUSH elements, as shown in Fig. 4. Each RBE2 element was connected by a zero-length CBUSH element, where the stiffness of each fastened joint could be defined in the FEA software, as shown in Table 5. This method allowed for modeling of the imperfect, non-rigid interface between the two half-cylinders and the cantilever plate.

The constraints on the structure were defined in the simulation model, as shown in Fig. 5. At the lower mounting

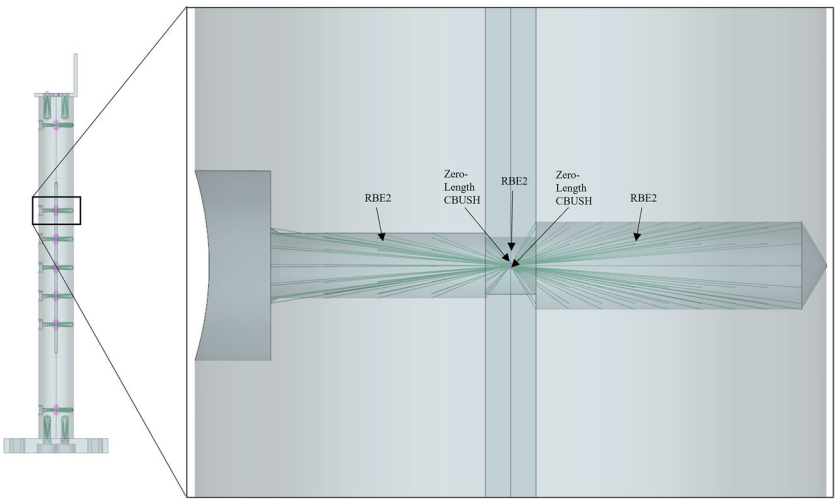

Fig. 4 A side view of the CAD model (with the cantilever plate facing out of the page) with a close-up inset view showing the RBE2 and zero-length CBUSH elements used to model the fasteners

Table 5 The FEM CBUSH stiffness values used in the FEA simulation to model the fasteners

CBUSH Stiffness	Half-Cylinder to Half-Cylinder Fasteners	Lower Mounting Bracket to Cylinder Fasteners	Upper Mounting Bracket to Cylinder Fasteners
X Translation	1751268.35 N/m	5253805.04 N/m	5253805.04 N/m
Y Translation	1751268.35 N/m	5253805.04 N/m	5253805.04 N/m
Z Translation	1751268.35 N/m	35025366.93 N/m	35025366.93 N/m
X Rotation per Radian	1751268.35 N/m	1751268.35 N/m	1751268.35 N/m
Y Rotation per Radian	1751268.35 N/m	1751268.35 N/m	1751268.35 N/m
Z Rotation per Radian	1751268.35 N/m	1751268.35 N/m	1751268.35 N/m

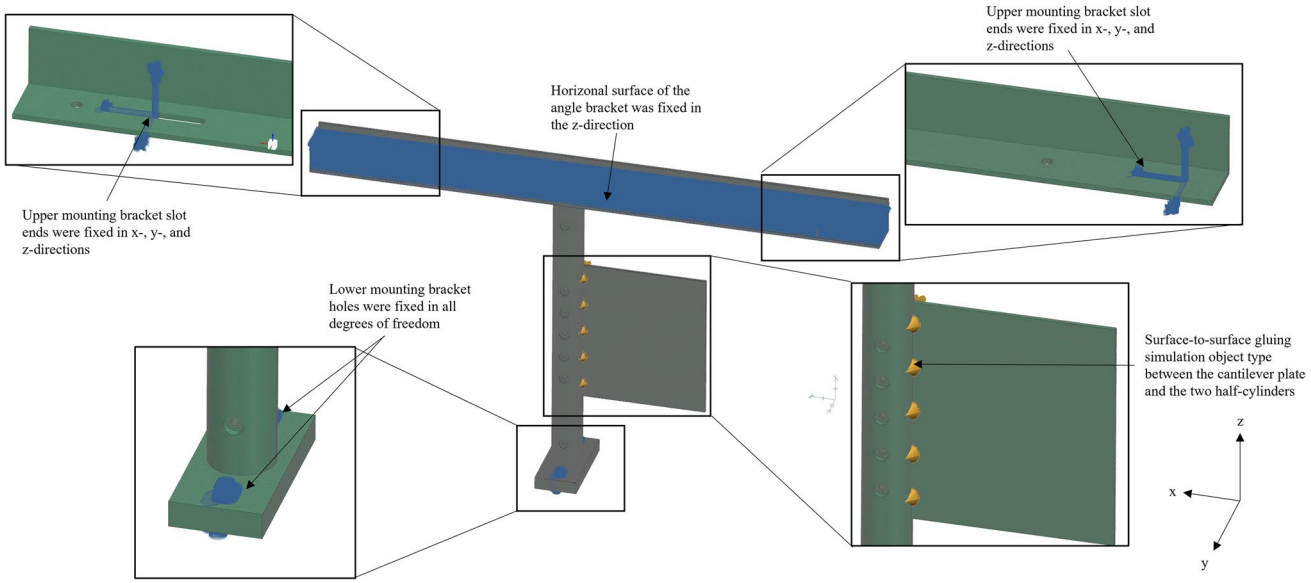

Fig. 5 The simulation model showing the constraints and the surface-to-surface gluing simulation object between the cantilever plate and the two half-cylinders

bracket, the holes were fixed in all degrees of freedom. At the upper mounting bracket, the slot ends were fixed in the x-, y-, and z-directions. Additionally, the horizonal surface of the angle bracket was fixed in the z-direction. The surface-to-surface gluing simulation object type was used to mate one surface of the cantilever plate to the corresponding surface of one of the half-cylinders, and the opposite surface of the cantilever plate to the corresponding surface of the other half-cylinder, as shown in Fig. 5. Structural damping and air damping were not modeled in the FEA.

The simulation was run, and the first eight natural frequencies and mode shapes of the structure were captured. To allow for direct comparison with the EMA results, 25 FEM nodes were selected in the FEA at the same location as those of the roving impact hammer hits used in the EMA method. The eigenvectors at these 25 nodes were extracted for use in MAC value calculations between the EMA and FEA results using a MATLAB script. For comparison of the ODS analysis and FEA results, the eigenvectors at these 25 FEM nodes were extracted for use in MAC value calculations using a MATLAB script. Again, note that the in-plane mode shape, 4*, was not considered in the analyses comparing each technique.

EMA Experimental Setup

All experimental setup parts were machined per the nominal design values and assembled using common tools. All CAD model and FEA analyses were performed with nominal dimensions. However, to account for tolerances in the two half-cylinder slots and ensure proper clamping of the cantilever plate, one stainless steel shim of thickness 0.100 mm was added to the near side surface of the cantilever plate next to each fastener hole, for a total of six shims across the clamping interface between the cantilever plate and one half-cylinder. In this paper, the near side of the cantilever plate is defined as the side of the cantilever plate facing out of the page in Fig. 6 and the far side of the cantilever plate is defined as the side of the cantilever plate facing into the page in Fig. 6.

The assembly was prepared for the roving hammer test by using a total of 37 impact locations, or nodes, for the EMA: 25 on the cantilever plate, 4 on the cylinder, 5 on the upper-cylinder mounting bracket, and 3 on the lower-cylinder mounting bracket, as shown in Fig. 6. A five-by-five grid of 25 points was precisely drawn on both sides of the cantilever plate as the reference locations for the EMA impact hammer hits on the near side, and for accelerometer placement on the far side. The remaining 12 points were precisely drawn on each side of the cylinder, and upper- and lower-cylinder mounting brackets as the reference locations for the EMA impact hammer hits on the near side, and for accelerometer placement on the far side.

The finished structure was then installed into the AEROLAB Educational Wind Tunnel using common tools. To gain a complete understanding of the structure's natural frequencies and mode shapes in the out-of-plane direction, one PCB Piezotronics, Inc. 352C66 single-axis accelerometer was placed on the far side of each component of the structure to measure the out-of-plane vibration, as denoted by the red circles in Fig. 6. A driving point survey was performed according to Siemens guidelines and recommendations in

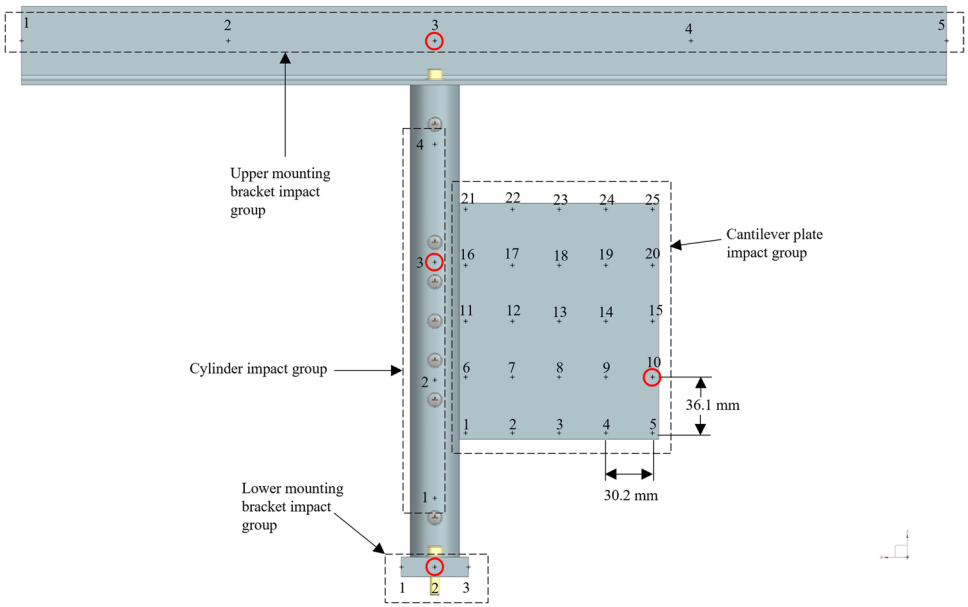

Fig. 6 The 37 hammer impact locations (denoted by cross-hairs) on the near side of the structure and broken out into 4 separate impact hammer test groups, and the 4 accelerometer locations (denoted by red circles) on the far side of the structure

the article, "Modal Driving Point Survey: What's at Stake?", to determine the optimal accelerometer location on the cantilever plate such that the highest number of mode shapes could be observed. The experimental setup installed in the wind tunnel, and with accelerometers attached for the EMA, is shown in Fig. 7. Note that the five-by-five grid of 25 points can be seen on each side of the cantilever plate. The EMA was performed using an LMS International Signal Conditioning and Data Acquisition System (SCADAS) III (SC-316W), a PCB Piezotronics, Inc. modally tuned impact hammer (086C01) with a nylon tip, four PCB Piezotronics, Inc. accelerometers (352C66), four PCB Piezotronics, Inc. adhesive mounting bases (080A15), PCB Piezotronics, Inc. adhesive wax (080A109), and Siemens Testlab 18.2 software. Several components of the test equipment are shown in Fig. 8.

The Siemens Testlab 18.2 software impact settings were chosen using the software's suggested values based on several test impacts. The Testlab 18.2 software settings used are given in Table 6. A test geometry was built in Siemens Testlab 18.2 software to specify for the software: the hammer impact locations and the accelerometer locations. The nodes and accelerometer locations on the Siemens Testlab 18.2 software test geometry are shown in Fig. 9. Note that these nodes mimic the 37 impact points drawn onto each side of the structure, as shown in Fig. 6.

For the EMA, the roving hammer test was performed using the 37 impact locations, or nodes. Each node was

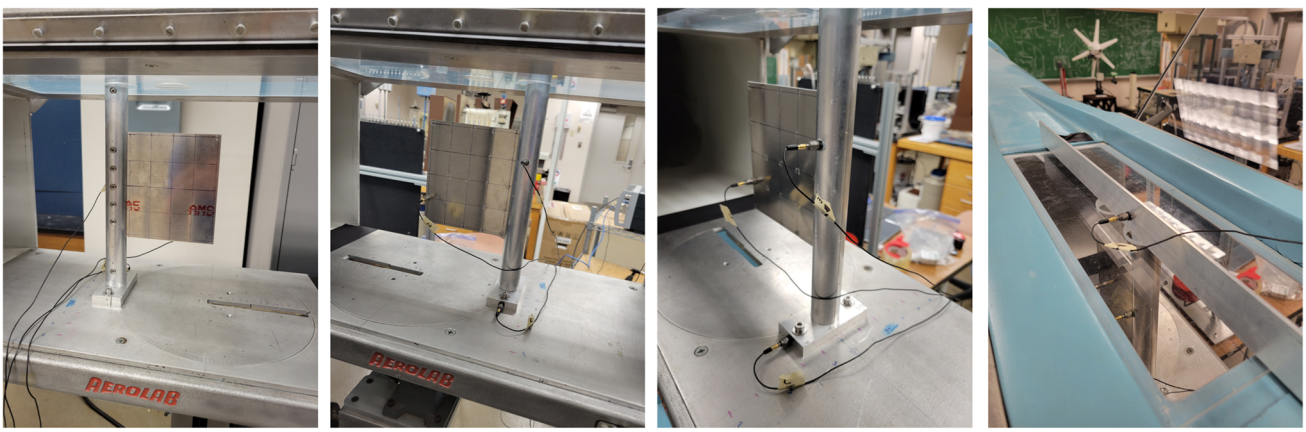

(a) (b) (c) (d)

Fig. 7 Photos of the experimental setup. From left to right: (**a**) the impact side of the cantilever plate, (**b**) the accelerometer side of the cantilever plate, (**c**) a close-up view of three of the accelerometers: one attached to the lower-cylinder mounting bracket, one attached to the cylinder, and one attached to the cantilever plate, and (**d**) a close-up view of the fourth accelerometer attached to the upper-cylinder mounting bracket

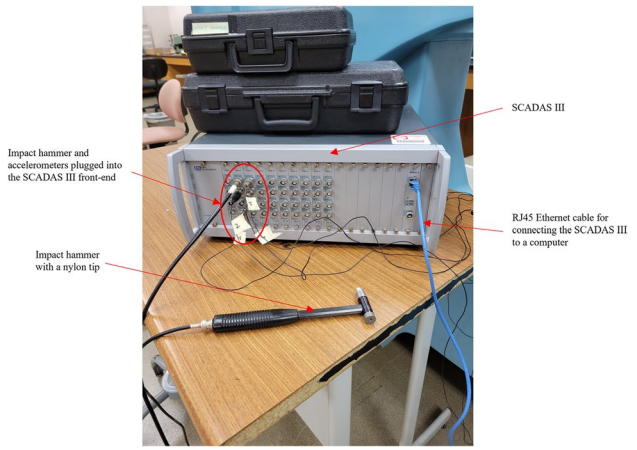

Fig. 8 Several components of the test equipment used in the EMA, including an LMS International SCADAS III (SC-316W) and a PCB Piezotronics, Inc. modally tuned impact hammer (086C01). The four PCB Piezotronics, Inc. accelerometers (352C66) and the PCB Piezotronics, Inc. modally tuned impact hammer were plugged into the front-end of the SCADAS III. The blue RJ45 Ethernet cable was plugged directly into a computer running Siemens Testlab 18.2 software

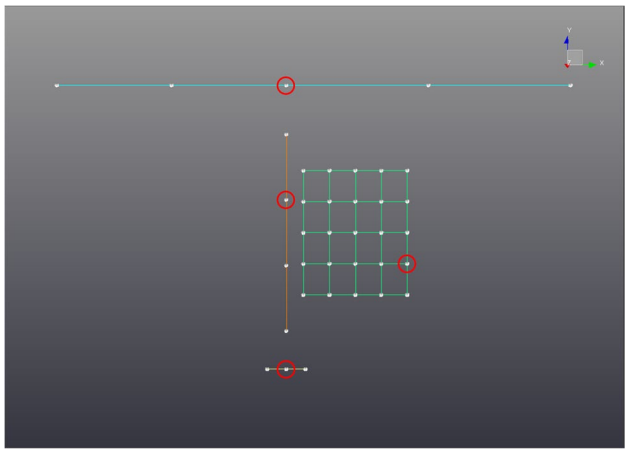

Fig. 9 The Siemens Testlab 18.2 software test geometry showing all roving hammer impact nodes (denoted by gray spheres) on the near side of the cantilever plate, cylinder, and upper- and lower-cylinder mounting brackets. Accelerometers were placed at the circled nodes on the far side of the structure

Table 6 Siemens Testlab 18.2 software "Impact Setup" menu test settings

Setting	Value
Input range	2 V
Trigger level	0.080 V
Pre-trigger	0.0025 s
Span	2500 Hz
Spectral lines	1600
Acquisition time	0.64 s
Resolution	1.56 Hz
Input exponential window	100% (no windowing)
Response exponential window	100% (no windowing)

impacted three times to compute an average of three FRFs, for a total of 111 hammer impacts on the structure. The cantilever plate impact group was tested first, then the cylinder impact group, followed by the lower-cylinder mounting bracket impact group, and finally the upper-cylinder mounting bracket impact group. All data, including natural frequencies, or eigenvalues, and mode shapes, or eigenvectors, were captured and stored by Siemens Testlab 18.2 software for post-processing. To allow for direct comparison with the FEA and ODS analysis results, the eigenvectors at the 25 cantilever plate nodes were extracted for use in MAC value calculations between the EMA and FEA methods and between the EMA and ODS analysis methods using MATLAB scripts. Lastly, previous experiments revealed that the roving accelerometer technique yielded poor results due to changes in mass loading between hammer impacts on the relatively thin cantilever plate. Therefore, roving accelerometer testing was not performed in this research.

ODS Analysis Experimental Setup

An ODS analysis of the cantilever plate was performed using a Correlated Solutions, Inc. high-speed DIC system, which is a non-contact optical measurement tool using stereo high-speed digital cameras that track speckle patterns on an object's surface. The equipment used was two Vision Research Phantom v2640 high-speed cameras with 2048 × 1952 pixel image resolution, two Tokina atx-i 100 mm F2.8 FF MACRO PLUS lenses with a focal length of 100 mm, all mounted on a Moog tripod, two HEDLER light-emitting diode (LED) lamps, a computer with an Advanced Micro Devices, Inc. Ryzen Threadripper 3970X central processing unit, a 128 GB Double Data Rate 4 memory, a 1 TB solid-state drive, an 8 TB hard disk drive, and the Correlated Solutions, Inc. VIC-3D Version 9.4.26, build 4081 software. The experimental setup with the high-speed DIC system is shown in Fig. 10.

The cantilever plate was prepared for ODS analysis testing by application of a thin coat of flat white paint on the near side, followed by a speckle pattern using an ink stamp with 0.33 mm dots from the Correlated Solutions, Inc. speckle kit, as shown in Figs. 11 and 12, where Fig. 11 shows a raw DIC image with two inset zoomed-in views showing the number of pixels per speckle. The five-by-five grid of 25 points on the opposite side of the cantilever plate was kept intact, to be used as a reference for the hammer impact location.

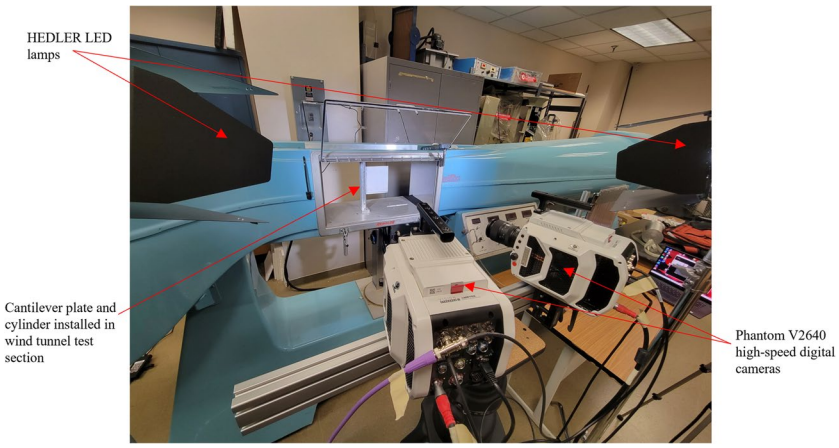

Fig. 10 Several components of the high-speed DIC system used in the ODS analysis testing, including two Vision Research Phantom v2640 high-speed digital cameras and two HEDLER LED lamps. The cantilever plate and the cylinder can be seen mounted in the wind tunnel test section

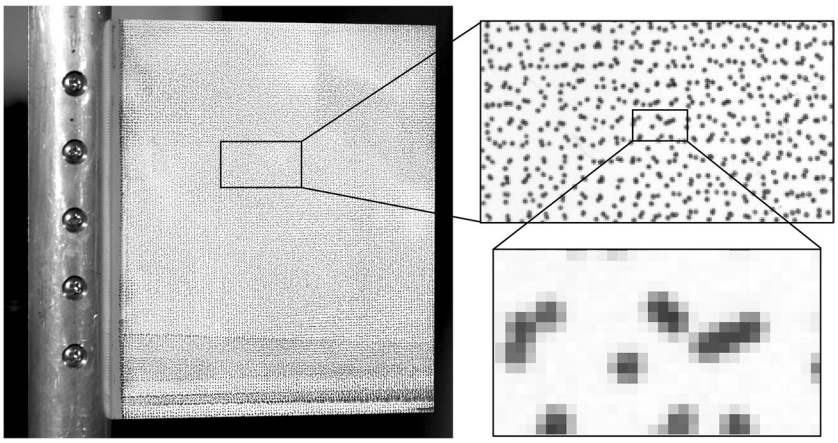

Fig. 11 The raw DIC image with two inset zoomed-in views showing the number of pixels per speckle. The speckle pattern was applied to the cantilever plate using an ink stamp with 0.33 mm dots

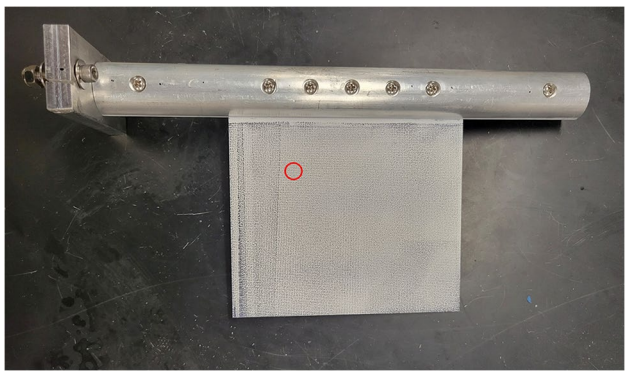

Fig. 12 The near side of the cantilever plate after application of a thin coat of flat white paint and the subsequent ink stamp speckle pattern. The hammer impact occurred at the circled location on the far side of the cantilever plate

Calibration of the DIC system was performed using a Correlated Solutions, Inc. calibration plate with feature spacing of 14 mm. A total of 38 calibration images were captured for the Correlated Solutions, Inc. correlation algorithm, one of which is shown in Fig. 13. A PCB Piezotronics, Inc. modally tuned impact hammer (086C01) with a nylon tip was used to impact the cantilever plate one time on the far side of point 7 in Fig. 6, as shown in Fig. 12, while the high-speed digital cameras recorded at 5000 frames per second (FPS). It is important to note that the ODS hammer impact occurred on the side of the cantilever plate opposite to the speckled surface, and opposite to the surface used in the EMA roving hammer test, so as not to interfere with the high-speed digital cameras' fields-of-view. The DIC parameters for this test, as reported by, or derived from, the VIC-3D software, are given in Table 7. Per Correlated Solutions, Inc., the VIC-3D software applies a perspective transform to the data which accounts for the shrinkage of the subset as it recedes from the camera. Then, an affine transfomation is applied to the perspective-corrected data. Measurement biases can be assumed to be zero (or negligible) due to the proper procedures for DIC system setup that were followed based on guidelines provided in the Correlated Solutions, Inc. "VIC-3D 9 Manual and Testing Guide". Per Correlated Solutions, Inc. documentation, "Minimizing Noise and Bias in 3D DIC", aliasing and contamination of the cameras' optics and sensors contribute to measurement biases. These issues were eliminated by ensuring that a quality and correctly sized speckle pattern was applied to the

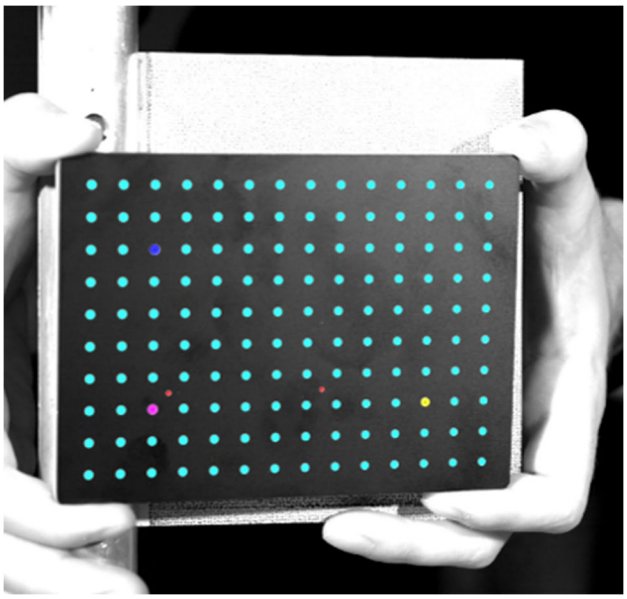

Fig. 13 One of the 38 calibration images that was captured by the DIC system for the Correlated Solutions, Inc. correlation algorithm. A Correlated Solutions Inc. calibration plate with feature spacing of 14 mm was used for the calibration

Table 7 Correlated Solutions, Inc. VIC-3D DIC software test parameters

Parameter	Value
Field-of-view (FOV)	196.391 mm width × 187.185 mm height
Average image scale between left and right cameras	10.4282 pixels/mm
Stereo-angle	25.2837°
Stand-off distance (SOD)	758.5 mm
Image acquisition rate	5000 FPS
Image filtering	None
Subset size	25 pixels or 2.3974 mm
Step size	7 pixels or 0.6712 mm
Subset shape function	Affine
Noise-floor (95% confidence interval)	0.003773 mm

test specimen, a good calibration was achieved, the cameras were not moved after calibration, and the cameras' optics and sensors were free of contamination.

The Correlated Solutions, Inc. VIC-3D Version 9.4.26, build 4081 software was not able to measure the excitation force from the impact hammer as a standalone unit, so FRFs were not generated because the excitation force from the impact hammer is required. However, researchers who wish to compute the FRFs may combine the Correlated Solutions, Inc. DIC system with the impact hammer attached to the SCADAS III. The response signal from the DIC system and the excitation signal from the impact hammer and SCADAS III could then be time-synced in post-processing to compute the FRFs. Furthermore, interested reseachers may note that Correlated Solutions, Inc. has stated that their DIC system will have the capability to measure the impact excitation force and compute FRFs in the next release of VIC-3D: Version 10. In the present work, the authors were interested in exploring the capabilities of each test method independently.

The ODS natural frequencies were estimated by first performing an FFT on the displacement versus time data captured by the high-speed DIC system to transform the data into the frequency domain. In the VIC-3D software's frequency analysis settings, a sampling step of 10 pixels was specified and a smoothing filter setting of 7 was applied. Then, for comparing acceleration FFTs between the EMA and ODS analysis methods, a frequency domain differentiation was performed on the ODS analysis displacement versus frequency data, and the EMA FRF was multiplied by an arbitrary force scaling factor to put both datasets in units of mm/s^2.

To allow for direct comparison of the ODS analysis results with the FEA and EMA results, a novel approach was employed. Eigenvectors were extracted from the collected ODS data at the 25 hammer impact points on the cantilever plate used for the EMA. To do this, the five-by-five grid of 25 hammer impact points from the EMA was precisely redrawn on the near side of the cantilever plate, as shown in Fig. 14(b). In the VIC-3D software's FFT workspace, points from 1 through 25 were selected by manually comparing speckles at the grid points in Fig. 14(b) to the image in the FFT workspace (Fig. 14(a)), a time-consuming but necessary process for acquiring accurate data for direct comparison with the FEA and EMA results. The eigenvectors at each of the 25 points for the first seven natural frequencies were identified and extracted for use in MAC value calculations between the ODS analysis and FEA results, and for use in MAC value calculations between the EMA and ODS analysis results using MATLAB scripts.

Results and Discussion

EMA and FEA Results

After completion of the roving hammer test, Siemens Testlab 18.2 software's PolyMAX algorithm calculated a curve fit of the captured FRFs. The first seven stable modes, which also appeared in the FEA results, were selected, as shown in Fig. 15. The first seven measured mode shapes from the EMA are shown in Fig. 16.

An AutoMAC calculation was performed on the first seven EMA mode shapes, as shown in Table 8. The EMA AutoMAC algorithm compares each EMA mode shape to

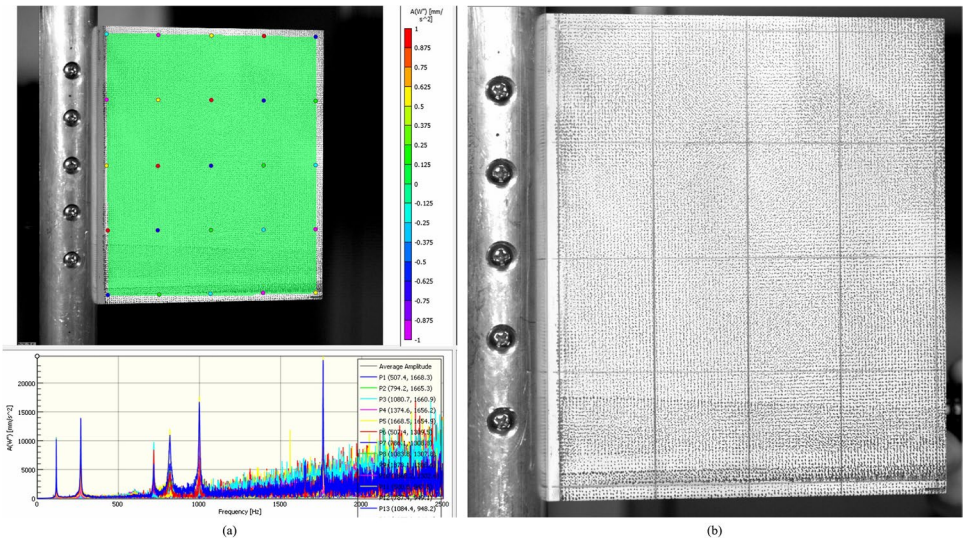

Fig. 14 The post-processing technique used for precisely picking the 25 grid points: (**a**) the precisely selected points in the VIC-3D software's FFT workspace, and (**b**) the precisely drawn five-by-five grid on the cantilever plate after high-speed DIC data collection

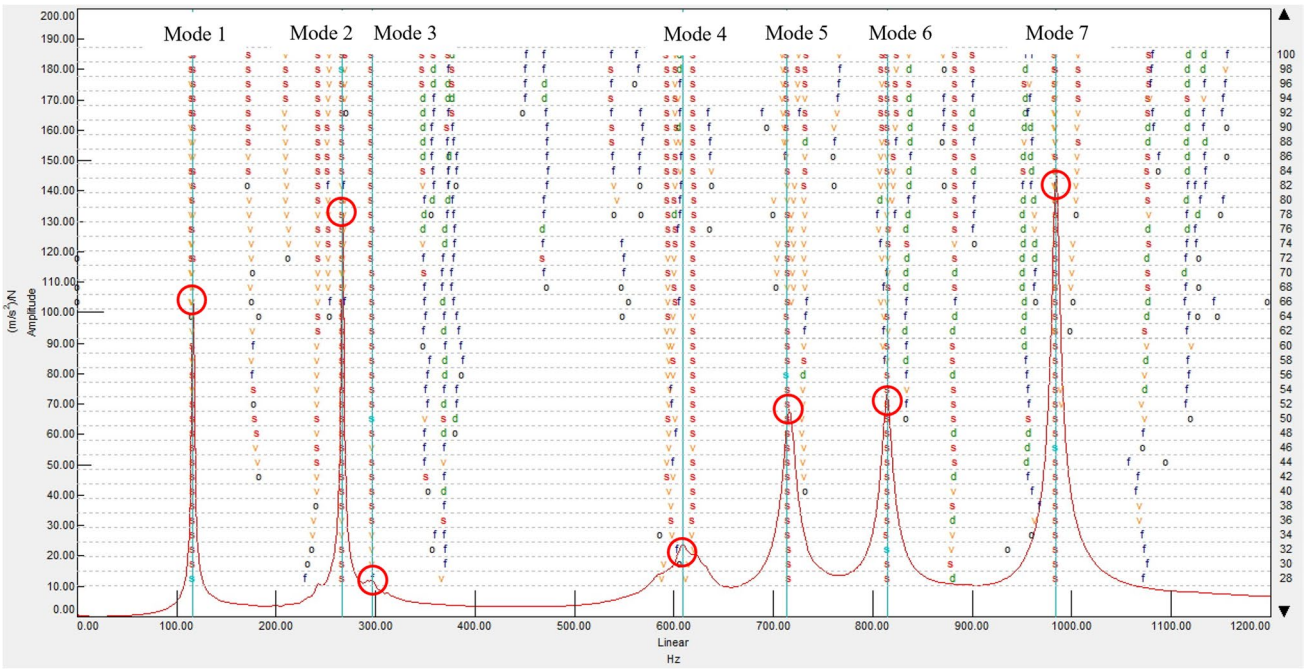

Fig. 15 The FRF curve fitting and stabilization diagram using the Siemens Testlab 18.2 software's PolyMAX algorithm. The first seven stable modes, which were also in the FEA results, were selected for analysis

itself and to all other EMA mode shapes in the dataset by computing a matrix of correlation values. The AutoMAC matrix can provide insight into the uniqueness of the mode shapes, whether there are closely spaced modes in the dataset, or whether there is spatial aliasing in the data. The AutoMAC matrix is always symmetric, with values of one along the diagonal, because mode shapes compared to themselves are correlated one-to-one. The AutoMAC and MAC matrices can be calculated using [14]

$$\mathrm{MAC}_{m,n} = \frac{\left|\{\varphi_m\}'\{\varphi_n\}\right|^2}{\left(\{\varphi_m\}'\{\varphi_m\}\right)\left(\{\varphi_n\}'\{\varphi_n\}\right)} \tag{2}$$

where $\{\varphi_m\}$ is the vector of eigenvectors from mode shape or ODS m, $\{\varphi_n\}$ is the vector of eigenvectors from mode shape or ODS n, and the prime symbol indicates the conjugate transpose of the vector. From the EMA AutoMAC matrix in Table 8 and the mode shapes in Fig. 16, it is obvious

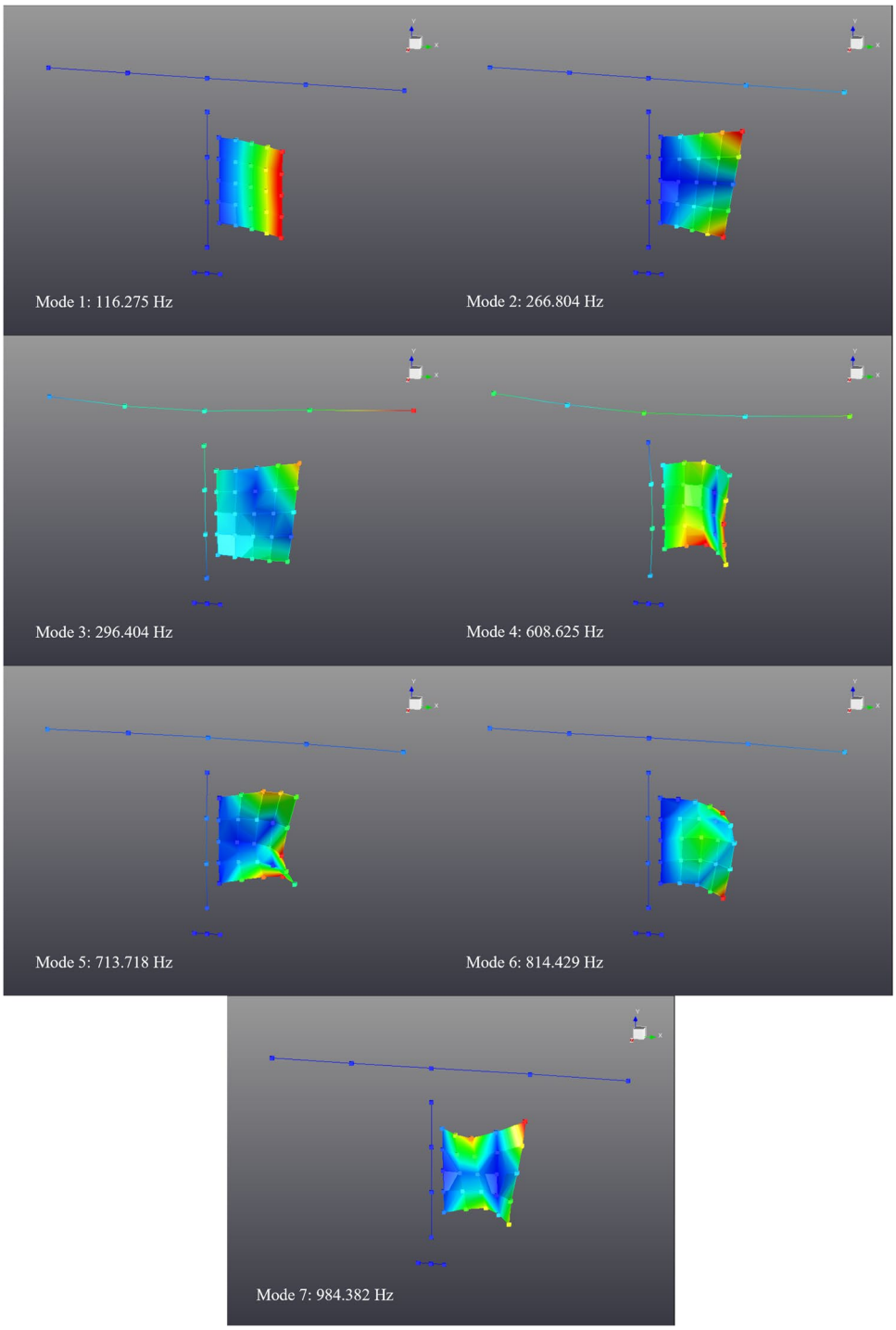

Fig. 16 The first seven mode shapes captured from the EMA using Siemens Testlab 18.2 software

that modes 2 and 3 had similar mode shapes, with a relatively high correlation value of 0.626. This high correlation resulted because modes 2 and 3 were closely spaced modes, with a frequency difference between them of only 29.6 Hz, which can be seen in the stabilization diagram of Fig. 15. Mode shapes 4 and 5 also exhibited a relatively high correlation value of 0.410, which can be attributed to the fact that the mode shapes had some similarities in bending. In Fig. 16, mode shape 4 has a single curved, symmetric shape in the out-of-plane direction. Mode shape 5 also exhibits this curved, symmetric shape near the horizontal centerline of the cantilever plate, but the upper and lower corners at the free end, opposite of the clamped end, bend in the opposite direction as that of the plate near the horizontal centerline. These similarities and differences in the mode shapes drive the correlation value of 0.410. All other off-diagonal

Table 8 The EMA AutoMAC values for the first seven cantilever plate mode shapes

EMA / EMA	Mode Shape 1	Mode Shape 2	Mode Shape 3	Mode Shape 4	Mode Shape 5	Mode Shape 6	Mode Shape 7
Mode Shape 1	1.000	0.005	0.062	0.026	0.011	0.102	0.007
Mode Shape 2	0.005	1.000	0.626	0.000	0.000	0.007	0.037
Mode Shape 3	0.062	0.626	1.000	0.204	0.028	0.098	0.106
Mode Shape 4	0.026	0.000	0.204	1.000	0.410	0.156	0.001
Mode Shape 5	0.011	0.000	0.028	0.410	1.000	0.123	0.002
Mode Shape 6	0.102	0.007	0.098	0.156	0.123	1.000	0.004
Mode Shape 7	0.007	0.037	0.106	0.001	0.002	0.004	1.000

AutoMAC values were 0.204 or less, demonstrating overall uniqueness among all other mode shapes.

The first eight mode shapes captured from the FEA are shown in Fig. 17. Note that mode 4* is an in-plane mode shape only, with no out-of-plane vibration. This mode 4* was not observable using the EMA technique, because there were no accelerometers taking measurements in the in-plane direction. As such, this mode was excluded from the analyses.

An AutoMAC calculation was also performed on the first seven FEA mode shapes, as shown in Table 9. From the FEA AutoMAC matrix in Table 9 and the mode shapes in Fig. 17, it is again obvious that modes 2 and 3 had similar mode shapes, with a relatively high correlation value of 0.770. This high correlation resulted because modes 2 and 3 were closely spaced modes, with a frequency difference between them of only 17.342 Hz. Mode shapes 4 and 5 also exhibited a relatively high correlation value of 0.613, which can be attributed to the fact that the mode shapes had some similarities in bending. In Fig. 17, mode shape 4 has a single curved, symmetric shape in the out-of-plane direction. Mode shape 5 also exhibits this curved, symmetric shape near the horizontal centerline of the cantilever plate, but the upper and lower corners at the free end, opposite of the clamped end, bend in the opposite direction as that of the plate near the horizontal centerline. These similarities and differences in the mode shapes drive the correlation value of 0.613. All other off-diagonal AutoMAC values were 0.156 or less, demonstrating overall uniqueness among all other mode shapes.

The EMA and FEA results were analyzed without accounting for the accelerometer and accelerometer wire masses in the FEA simulation. Table 10 presents the first seven natural frequencies of the cantilever plate, as captured by the EMA and FEA. The natural frequencies between the EMA and FEA results are compared with the percent difference calculation given by Equation 1. The percent differences between the EMA and FEA results were less than 4.8% for each natural frequency and the average percent difference of the first seven natural frequencies was 2.411%. Furthermore, a MAC value calculation was performed, which determines how well the EMA-based mode shapes correlate with the FEA-based mode shapes. The EMA mode shapes that were compared with their corresponding FEA mode shapes (diagonal elements in the MAC matrix) should be close to one, while the EMA mode shapes that were compared with different FEA mode shapes (off-diagonal elements in the MAC matrix) should be close to zero. The MAC values are presented in tabular form in Table 11. The MAC values on the diagonal were at least 0.845 and there was an average value on the diagonal of 0.940, meaning that the EMA results correlated very well with the FEA results.

It is interesting to note that FEA mode shape 3 was highly correlated with EMA mode shape 2, at 0.921, and EMA mode shape 3 had a high correlation of 0.408 with FEA mode shape 2. These high correlations are due to the closely spaced mode 2 and mode 3 of the structure, as was also seen in the EMA and FEA AutoMACs. As expected, the correlation between FEA mode shape 5 and EMA mode shape 4 was relatively high, at 0.576, and EMA mode shape 5 had a high correlation of 0.432 with FEA mode shape 4. Again, this is due to the similarities in bending between mode shape 4 and mode shape 5. All other off-diagonal MAC values were 0.322 or less, demonstrating overall uniqueness among all other mode shapes.

ODS Analysis and FEA Results

After completion of the single impact test with high-speed DIC, the Correlated Solutions, Inc. VIC-3D software performed an FFT of the time-series data. The displacement versus frequency data was exported to MATLAB where it was plotted, as shown in Fig. 18. The first seven cantilever plate ODSs were selected from the FFT plot using the peak-picking method. The first seven measured cantilever plate ODSs are shown in Fig. 19, and they match very well with the EMA-based mode shapes and the FEA-based mode shapes shown in Figs. 16 and 17, respectively. It is interesting to note that ODS 3 and ODS 4 did not have sharp peaks

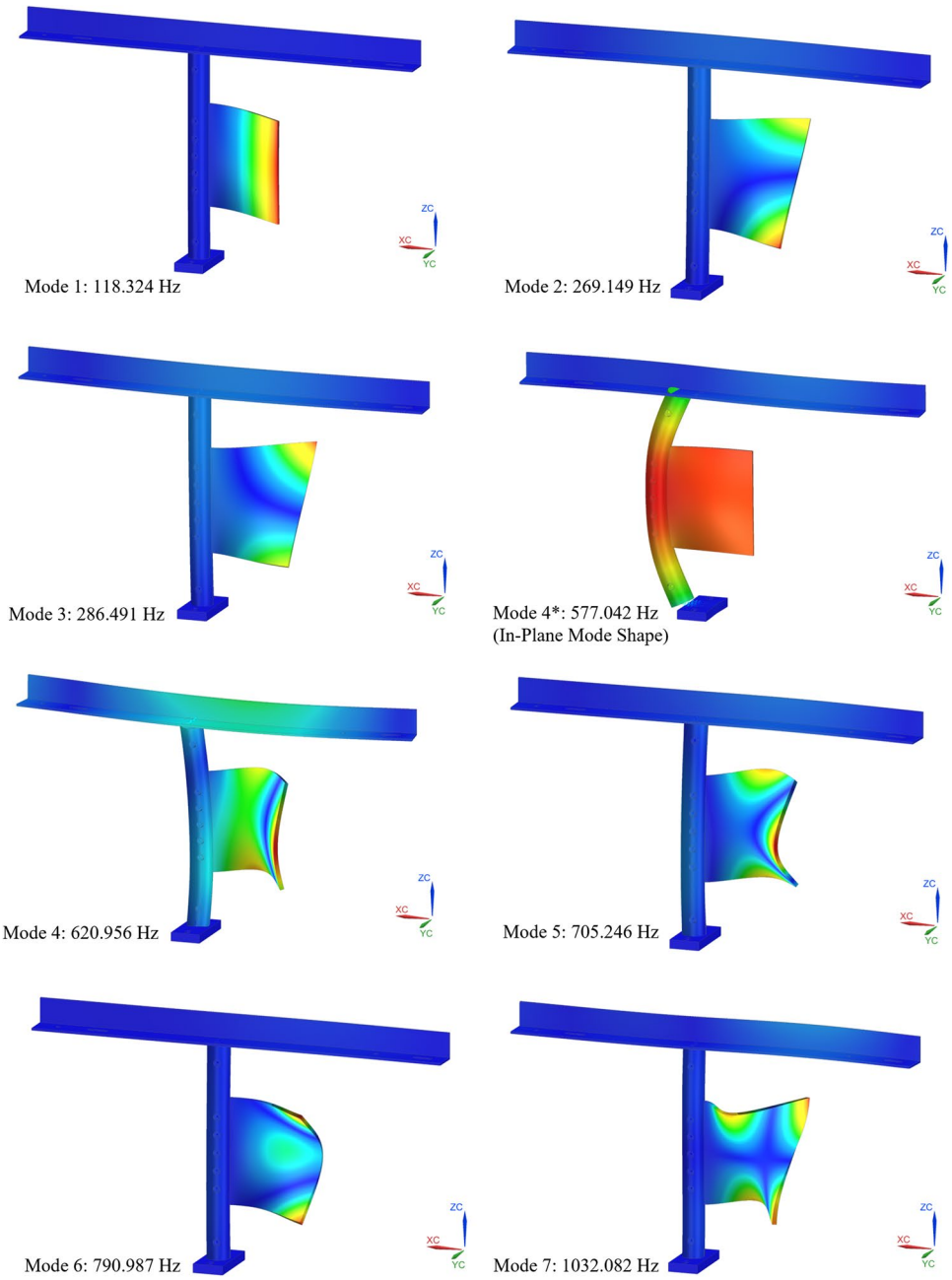

Fig. 17 The eight mode shapes captured from the FEA. Note that mode 4* is an in-plane mode shape only, with no vibration in the out-of-plane direction

Table 9 The FEA AutoMAC values for the first seven cantilever plate mode shapes

FEA / FEA	Mode Shape 1	Mode Shape 2	Mode Shape 3	Mode Shape 4	Mode Shape 5	Mode Shape 6	Mode Shape 7
Mode Shape 1	1.000	0.006	0.014	0.026	0.000	0.108	0.000
Mode Shape 2	0.006	1.000	0.770	0.043	0.005	0.004	0.028
Mode Shape 3	0.014	0.770	1.000	0.037	0.021	0.014	0.050
Mode Shape 4	0.026	0.043	0.037	1.000	0.613	0.027	0.008
Mode Shape 5	0.000	0.005	0.021	0.613	1.000	0.156	0.003
Mode Shape 6	0.108	0.004	0.014	0.027	0.156	1.000	0.001
Mode Shape 7	0.000	0.028	0.050	0.008	0.003	0.001	1.000

Table 10 The first seven natural frequencies of the cantilever plate determined by the EMA and FEA, and their percent differences

Natural Frequencies	EMA (Hz)	FEA (Hz)	Percent Difference (%)
1	116.275	118.324	1.747
2	266.804	269.149	0.875
3	296.404	286.491	3.401
4	608.625	620.956	2.006
5	713.718	705.246	1.194
6	814.429	790.987	2.920
7	984.382	1032.082	4.731

like the peaks identifying ODSs 1, 2, 5, 6, and 7, as shown in Fig. 18. For ODS 3, this phenomenon likely occurred because the speckle pattern was only applied to the cantilever plate and DIC was only performed on the cantilever plate. As a result, the displacements from the cylinder and the upper- and lower-cylinder mounting brackets were not contributors to the FFT of the ODS analysis displacement versus frequency data. For ODS 3 and ODS 4, where the peaks were not as well defined, the exact frequencies were selected where a good performance compromise of natural frequency percent differences and MAC values were yielded. Unlike the Siemens Testlab 18.2 software, the Correlated Solutions, Inc. VIC-3D Version 9.4.26, build 4081 software does not have a built-in curve fitting algorithm to aid in selecting ODSs.

An AutoMAC calculation was also performed on the first seven ODS analysis ODSs, as shown in Table 12. From the ODS analysis AutoMAC matrix in Table 12 and the ODSs in Fig. 19, it is again obvious that ODSs 2 and 3 had similar ODSs, with a relatively high correlation value of 0.828. This high correlation resulted because ODSs 2 and 3 were closely spaced ODSs, with a frequency difference between them of only 17.778 Hz, which can be seen in the FFT plot of Fig. 18. ODSs 4 and 5 exhibited a correlation value of 0.196, which can be attributed to the fact that the ODSs had some similarities in bending. In Fig. 19, ODS 4 has a single curved, symmetric shape in the out-of-plane direction. ODS 5 also exhibits this curved, symmetric shape near the horizontal centerline of the cantilever plate, but the upper and lower corners at the free end, opposite of the clamped end, bend in the opposite direction as that of the plate near the horizontal centerline. These similarities and differences in the ODSs drive the correlation value of 0.196. All other off-diagonal AutoMAC values were 0.224 or less, demonstrating overall uniqueness among all other ODSs.

Table 13 presents the first seven natural frequencies of the cantilever plate, as captured by the ODS analysis and FEA. The percent differences between the ODS analysis and FEA results were less than 3.4% for each natural frequency and the average percent difference of the first seven natural frequencies of the cantilever plate was 1.620%. A MAC value calculation was performed between the ODS analysis ODSs and the FEA-based mode shapes of the cantilever plate and the MAC values on the diagonal were at least 0.728 and had an average value on the diagonal of 0.886. The MAC values

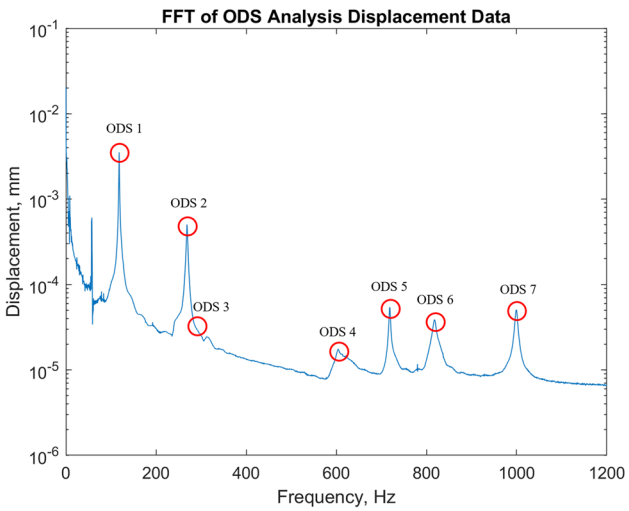

Fig. 18 The displacement versus frequency plot of the cantilever plate captured using high-speed DIC. The frequencies at the circled peaks indicate the cantilever plate's first seven natural frequencies

Table 11 The MAC values between the EMA and FEA results for the first seven cantilever plate mode shapes

EMA / FEA	Mode Shape 1	Mode Shape 2	Mode Shape 3	Mode Shape 4	Mode Shape 5	Mode Shape 6	Mode Shape 7
Mode Shape 1	0.998	0.008	0.070	0.022	0.014	0.104	0.009
Mode Shape 2	0.010	0.939	0.408	0.032	0.003	0.004	0.019
Mode Shape 3	0.011	0.921	0.845	0.048	0.008	0.042	0.070
Mode Shape 4	0.030	0.001	0.189	0.987	0.432	0.138	0.004
Mode Shape 5	0.000	0.001	0.074	0.576	0.929	0.031	0.017
Mode Shape 6	0.103	0.001	0.048	0.035	0.322	0.918	0.021
Mode Shape 7	0.000	0.035	0.060	0.017	0.005	0.006	0.964

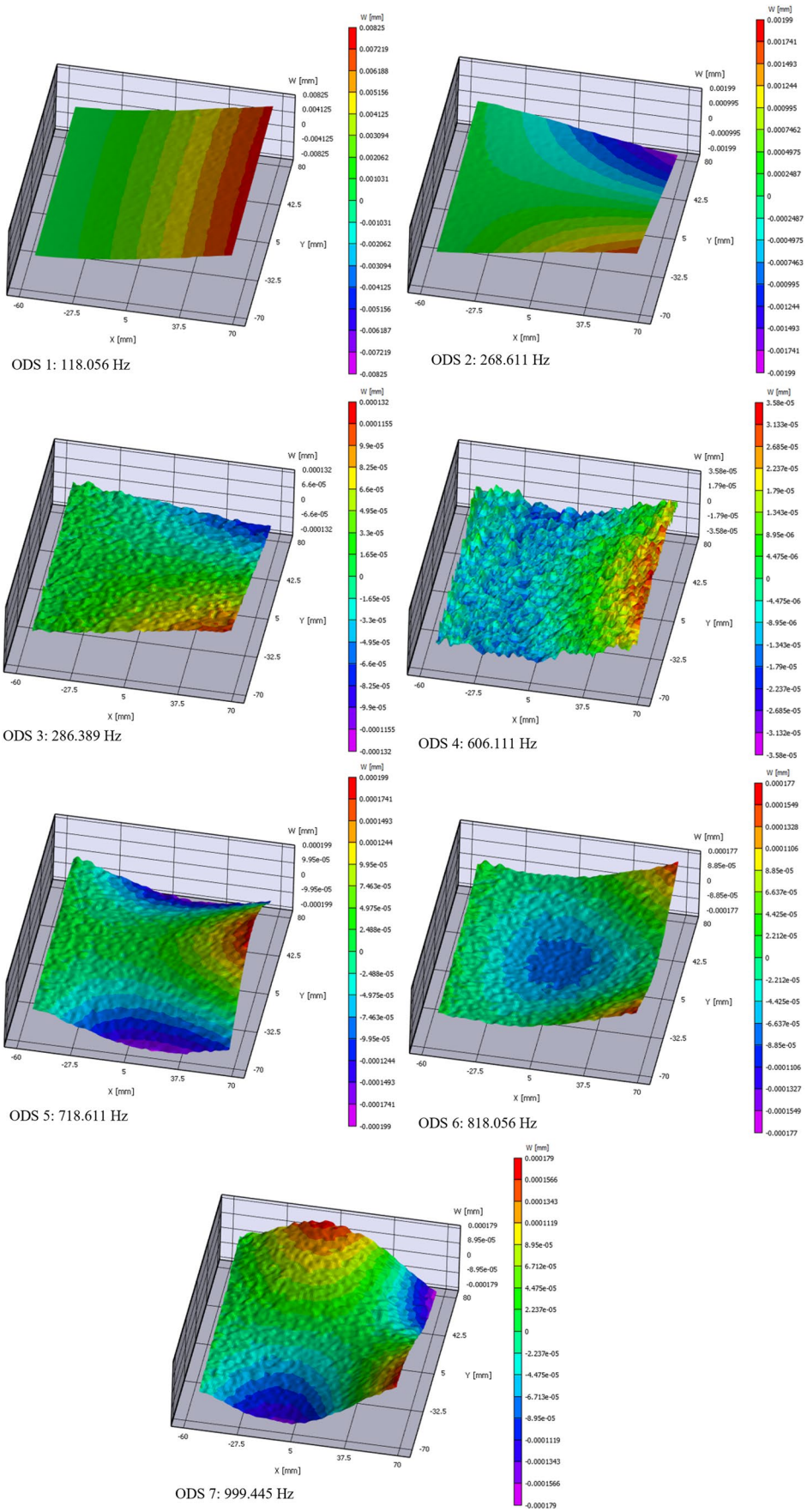

Fig. 19 The ODSs for the first seven cantilever plate natural frequencies captured using high-speed DIC

Table 12 The ODS analysis AutoMAC values for the first seven cantilever plate ODSs

ODS Analysis / ODS Analysis	ODS 1	ODS 2	ODS 3	ODS 4	ODS 5	ODS 6	ODS 7
ODS 1	1.000	0.001	0.114	0.140	0.011	0.174	0.003
ODS 2	0.001	1.000	0.828	0.006	0.001	0.000	0.046
ODS 3	0.114	0.828	1.000	0.068	0.010	0.017	0.057
ODS 4	0.140	0.006	0.068	1.000	0.196	0.224	0.003
ODS 5	0.011	0.001	0.010	0.196	1.000	0.104	0.000
ODS 6	0.174	0.000	0.017	0.224	0.104	1.000	0.001
ODS 7	0.003	0.046	0.057	0.003	0.000	0.001	1.000

Table 13 The first seven natural frequencies of the cantilever plate determined by the ODS analysis and FEA, and their percent differences

Natural Frequencies	ODS Analysis (Hz)	FEA (Hz)	Percent Difference (%)
1	118.056	118.324	0.227
2	268.611	269.149	0.200
3	286.389	286.491	0.036
4	606.111	620.956	2.420
5	718.611	705.246	1.877
6	818.056	790.987	3.365
7	999.445	1032.082	3.213

are presented in tabular form in Table 14. The MAC values show that there was overall good correlation between the ODSs captured using high-speed DIC and the mode shapes captured from the FEA.

It is interesting to note that FEA mode shape 3 was highly correlated with ODS analysis ODS 2, at 0.938, and ODS analysis ODS 3 had a high correlation of 0.788 with FEA mode shape 2. These high correlations are due to the closely spaced mode 3 and ODS 2, and ODS 3 and mode 2 of the structure, as was also seen in the ODS analysis and FEA AutoMACs. As expected, the correlation between FEA mode shape 5 and ODS analysis ODS 4 was relatively high, at 0.317, and ODS analysis ODS 5 had a high correlation of 0.391 with FEA mode shape 4. Again, this is due to the similarities in bending between mode shape 5 and ODS 4, and similarly between ODS 5 and mode shape 4. All other off-diagonal MAC values were 0.381 or less, demonstrating overall uniqueness among all other mode shapes and ODSs.

EMA and ODS Analysis Results

To allow for direct comparison of the acceleration versus frequency FFT plots between the EMA and ODS analysis methods, the EMA FRF was multipled by an arbitrary scaling force factor of 0.015 N to convert its units from (mm/s^2)/N to mm/s^2. Then, on the ODS analysis displacement versus frequency FFT, a frequency domain differentiation was performed by mulitiplying the ODS analysis displacement signal by the square of the angular frequency, ω^2, to convert to the acceleration signal in the frequency domain. The results are plotted for comparison in Fig. 20, and as expected, the EMA and ODS analysis acceleration versus frequency curves agree well.

Table 15 presents the first seven natural frequencies of the cantilever plate, as captured by the EMA and ODS analysis. The percent differences between the EMA and ODS analysis results were less than 3.5% for each natural frequency and the average percent difference of the first seven natural frequencies of the cantilever plate was 1.242%. Furthermore, a MAC value calculation was performed between the EMA-based mode shapes and the ODS analysis ODSs of the cantilever plate and the MAC

Table 14 The MAC values between the ODS analysis and FEA results for the first seven cantilever plate ODSs and mode shapes, respectively

FEA / ODS Analysis	Mode Shape 1	Mode Shape 2	Mode Shape 3	Mode Shape 4	Mode Shape 5	Mode Shape 6	Mode Shape 7
ODS 1	1.000	0.006	0.013	0.027	0.000	0.110	0.000
ODS 2	0.001	0.937	0.938	0.000	0.002	0.001	0.036
ODS 3	0.112	0.788	0.763	0.007	0.010	0.004	0.035
ODS 4	0.141	0.035	0.045	0.728	0.317	0.061	0.001
ODS 5	0.012	0.004	0.005	0.391	0.911	0.381	0.001
ODS 6	0.170	0.019	0.014	0.188	0.008	0.873	0.001
ODS 7	0.003	0.035	0.061	0.004	0.006	0.000	0.990

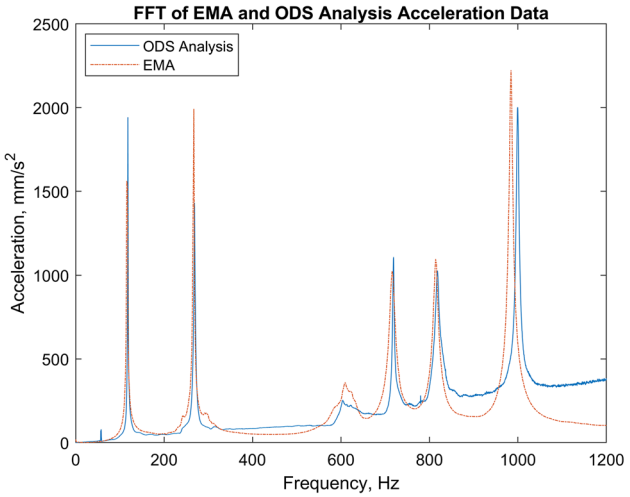

Fig. 20 The acceleration versus frequency plots of the cantilever plate captured using the EMA and ODS analysis techniques. The EMA signal was multiplied by an arbitrary scaling force factor of 0.015 N. The ODS analysis displacement signal was multiplied by ω^2 to convert to the acceleration signal in the frequency domain

Table 15 The first seven natural frequencies of the cantilever plate determined by the EMA and ODS analysis, and their percent differences

Natural Frequencies	EMA (Hz)	ODS Analysis (Hz)	Percent Difference (%)
1	116.275	118.056	1.520
2	266.804	268.611	0.675
3	296.404	286.389	3.437
4	608.625	606.111	0.414
5	713.718	718.611	0.683
6	814.429	818.056	0.444
7	984.382	999.445	1.518

values on the diagonal were at least 0.505 and had an average value on the diagonal of 0.862. The MAC values are presented in tabular form in Table 16. The MAC values show that there was overall good correlation between the mode shapes captured using the EMA and the ODSs captured from high-speed DIC.

It is interesting to note that EMA mode shape 2 was highly correlated with ODS analysis ODS 3, at 0.764, and ODS analysis ODS 2 had a high correlation of 0.652 with EMA mode shape 3. These high correlations are due to the closely spaced mode 2 and ODS 3, and ODS 2 and mode 3 of the structure, as was also seen in the EMA and ODS analysis AutoMACs. As expected, the correlation between ODS analysis ODS 5 and EMA mode shape 4 was relatively high, at 0.356, and ODS analysis ODS 4 had a high correlation of 0.181 with EMA mode shape 5. Again, this is due to the similarities in bending between ODS 5 and mode shape 4, and similarly between ODS 4 and mode shape 5. All other off-diagonal MAC values were 0.229 or less, demonstrating overall uniqueness among all other mode shapes and ODSs.

Existence of the 577.042 Hz In-Plane Mode Shape

The in-plane mode shape at 577.042 Hz was observed in the FEA results (mode 4*), as shown in Fig. 21. This mode, or ODS, was not observed in the EMA or ODS analysis results, respectively, because the EMA and ODS analysis methods only measured the out-of-plane vibration. In the EMA method, the out-of-plane vibration of the cantilever plate, cylinder, and upper- and lower-cylinder mounting brackets were measured, and in the ODS analysis method, the out-of-plane vibration of the cantilever plate was measured. It is interesting to note from Fig. 21 that the cylinder undergoes large in-plane bending, while the cantilever plate experiences only in-plane translation.

Conclusion

The purpose of this work was to employ experimental techniques on a cantilever plate in a wind tunnel by performing EMA and ODS analysis methods in the lab and comparing the results to FEA results. A detailed CAD model of the experimental setup was first introduced, including a novel

Table 16 The MAC values between the EMA and ODS analysis results for the first seven cantilever plate mode shapes and ODSs, respectively

EMA / ODS Analysis	Mode Shape 1	Mode Shape 2	Mode Shape 3	Mode Shape 4	Mode Shape 5	Mode Shape 6	Mode Shape 7
ODS 1	0.998	0.007	0.070	0.023	0.014	0.107	0.010
ODS 2	0.000	0.989	0.652	0.001	0.001	0.010	0.039
ODS 3	0.126	0.764	0.505	0.009	0.012	0.001	0.032
ODS 4	0.146	0.000	0.229	0.697	0.181	0.149	0.011
ODS 5	0.010	0.000	0.022	0.356	0.956	0.173	0.000
ODS 6	0.168	0.000	0.073	0.193	0.079	0.938	0.028
ODS 7	0.005	0.042	0.070	0.011	0.002	0.008	0.953

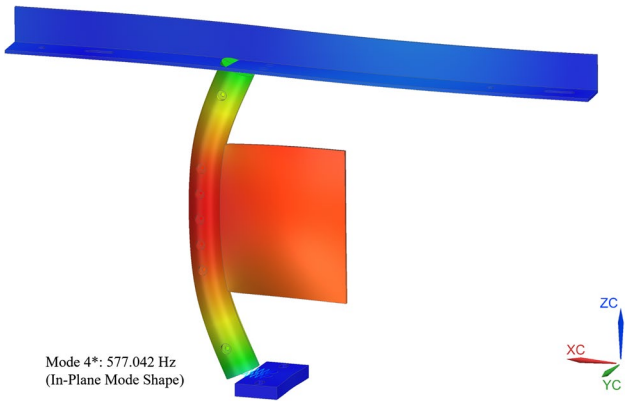

Fig. 21 The in-plane mode shape at 577.042 Hz as captured by FEA. This mode, or ODS, was not measured by the EMA or ODS analysis, respectively, because the EMA and ODS analysis methods measured out-of-plane vibration only

cylinder design which allowed for clamping of the cantilever plate while ensuring that there was no gap between the two half-cylinders. The FEM and simulation setup were discussed, including a mesh element size convergence study, mesh parameters, fastener stiffnesses defined by RBE2 and CBUSH elements, and boundary conditions, allowing for accurate modeling of the non-rigid interface between the two half-cylinders and the cantilever plate. Then, the experimental setup was introduced, including the impact hammer with the accelerometer equipment as well as the high-speed DIC system.

The results and analyses using each experimental method were presented and compared with the FEA results. A novel post-processing technique for comparing the mode shapes captured using the EMA or FEA with the ODSs captured using high-speed DIC by extracting eigenvectors at the EMA hammer impact locations was introduced. This method required precisely selecting points within the Correlated Solutions, Inc. VIC-3D software of the ODS analysis and selecting nodes within the Siemens NX Pre/Post application FEA software at the precise EMA hammer impact locations.

The percent differences between the EMA-based and FEA-based results were less than 4.8% for each natural frequency and the average percent difference of the first seven natural frequencies of the cantilever plate was 2.411%. The MAC values between the EMA-based mode shapes and FEA-based mode shapes were at least 0.845 for each corresponding mode shape on the diagonal of the MAC matrix and there was an average value on the diagonal of 0.940. The percent differences between the ODS analysis and FEA results were less than 3.4% for each natural frequency and the average percent difference of the first seven natural frequencies of the cantilever plate was 1.620%. The MAC values between the ODS analysis ODSs and FEA-based mode shapes were at least 0.728 for each corresponding ODS and mode shape on the diagonal of the MAC matrix and there was an average value on the diagonal of 0.886. The percent differences between the EMA and ODS analysis results were less than 3.5% for each natural frequency and the average percent difference of the first seven natural frequencies of the cantilever plate was 1.242%. The MAC values between the EMA-based mode shapes and ODS analysis ODSs were at least 0.505 for each corresponding mode shape and ODS on the diagonal of the MAC matrix and there was an average value on the diagonal of 0.862.

The results of the FEA, EMA, and ODS analysis methods showed that mode shapes and ODSs 2 and 3 were highly correlated. These two modes and ODSs were closely spaced in frequency, and it is easy to see their similarities in Figs. 16, 17, and 19. The results also showed that mode shapes and ODSs 4 and 5 had a relatively high correlation. From viewing the mode shapes and ODSs in Figs. 16, 17, and 19, the similarities in bending between these two mode shapes and ODSs that drives the relatively high correlation becomes apparent. An in-plane mode shape at 577.042 Hz in the FEA results was not observed in the EMA or ODS analysis results. The mode shape exhibited in-plane bending of the cylinder, but little to no bending of any other component in the experimental setup. If this mode shape is an experimental mode of interest, researchers may place accelerometers on the experimental setup in the in-plane direction and carry out an EMA in the in-plane direction. Overall, both the EMA and ODS analysis methods yielded excellent results that agreed well with the FEA results. Both methods are highly capable of measuring their respective mode shapes and ODSs. However, in the case of the ODS analysis, if the researcher is interested in obtaining FRFs rather than FFTs, combining the response measurements from the DIC system with the input force measurement from a separate data acquisition system is necessary, as in Witt and Rohe [24] or Frankovský et al. [25]. Although the EMA method may be considered a turnkey solution for obtaining FRFs, Correlated Solutions, Inc. has stated that their DIC system will be capable of computing FRFs in the next release of VIC-3D: Version 10. This added capability would make the DIC system a standalone turnkey solution for computing FRFs in an EMA. The results of this work serve as a foundation for future research in FSI of a cantilever plate immersed in air flow inside a wind tunnel.

Acknowledgements The authors would like to thank the National Science Foundation for their support under grant numbers 1763024 and 2117732, the latter of which allowed the authors to purchase a high-speed DIC system. They would also like to thank Frank Poradek, Chris Sensor, and Peter Schaldenbrand at Siemens for their technical support with the LMS International SCADAS III and Testlab 18.2 software. The authors would like to thank Alistair Tofts and Micah Simonsen at Correlated Solutions, Inc. for their training and technical assistance with high-speed DIC testing. The authors would also like to thank

Northrop Grumman Corporation for allowing them to use the Siemens NX CAD software for this research.

Author Contributions All authors contributed to the study conception and design. Project administration, funding acquisition, provision of resources, and supervision were performed by Weidong Zhu. Material preparation, data collection, and analysis were performed by David T. Will. The first draft of the manuscript was written by David T. Will and it was revised by Weidong Zhu. All authors read and approved the final manuscript.

Data Availability Available upon request.

Declarations

Competing Interests On behalf of all authors, the corresponding author states that there is no conflict of interest.

References

1. Wu J, Shu C, Zhao N (2014) Numerical study of flow control via the interaction between a circular cylinder and a flexible plate. J Fluids Struct. https://doi.org/10.1016/j.jfluidstructs.2014.06.002
2. Duan F, Wang J (2021) Fluid–structure–sound interaction in noise reduction of a circular cylinder with flexible splitter plate. J Fluid Mech. https://doi.org/10.1017/jfm.2021.403
3. Oruç V (2016) Strategies for the applications of flow control downstream of a bluff body. Flow Meas Instrum. https://doi.org/10.1016/j.flowmeasinst.2016.08.008
4. Balint TS, Lucey AD (2005) Instability of a cantilevered flexible plate in viscous channel flow. J Fluids Struct. https://doi.org/10.1016/j.jfluidstructs.2005.05.005
5. Yu Y, Liu Y (2015) Flapping dynamics of a piezoelectric membrane behind a circular cylinder. J Fluids Struct. https://doi.org/10.1016/j.jfluidstructs.2015.03.009
6. Bleischwitz R, de Kat R, Ganapathisubramani B (2016) Aeromechanics of membrane and rigid wings in and out of ground-effect at moderate Reynolds Numbers. J Fluids Struct. https://doi.org/10.1016/j.jfluidstructs.2016.02.005
7. Meirovitch L (1997) Principles and Techniques of Vibrations. Prentice-Hall Inc, Upper Saddle River
8. Inman DJ (2014) Engineering Vibrations, 4th edn. Pearson Education Inc, Upper Saddle River
9. Szilard R (2004) Theories and Applications of Plate Analysis: Classical, Numerical and Engineering Methods. John Wiley & Sons Inc, Hoboken
10. Warburton GB (1954) The vibration of rectangular plates. Proceedings of the Institution of Mechanical Engineers. https://doi.org/10.1243/PIME_PROC_1954_168_040_02
11. Leissa W (1973) The free vibration of rectangular plates. J Sound Vib. https://doi.org/10.1016/S0022-460X(73)80371-2
12. Warren C, Niezrecki C, Avitabile P, Pingle P (2011) Comparison of FRF measurements and mode shapes determined using optically image based, laser, and accelerometer measurements. Mech Syst Signal Process. https://doi.org/10.1016/j.ymssp.2011.01.018
13. Kalybek M, Bocian M, Pakos W, Grosel J, Nikitas N (2021) Performance of camera-based vibration monitoring systems in input-output modal identification using shaker excitation. Remote Sens. https://doi.org/10.3390/rs13173471
14. Ewins DJ (2000) Modal Testing: Theory, Practice and Application, 2nd edn. Research Studies Press Ltd., Baldock
15. Hu Y, Guo W, Zhu W, Xu Y (2019) Local damage detection of membranes based on Bayesian operational modal analysis and three-dimensional digital image correlation. Mech Syst Signal Process. https://doi.org/10.1016/j.ymssp.2019.04.051
16. Xu YF, Chen D-M, Zhu WD (2017) Damage identification of beam structures using free response shapes obtained by use of a continuously scanning laser Doppler vibrometer system. Mech Syst Signal Process. https://doi.org/10.1016/j.ymssp.2016.12.042
17. Gwashavanhu B, Oberholster AJ, Heyns PS (2016) Rotating blade vibration analysis using photogrammetry and tracking laser Doppler vibrometry. Mech Syst Signal Process. https://doi.org/10.1016/j.ymssp.2016.02.019
18. Gülbahçe E, Çelik M (2021) Experimental modal analysis for the plate structures with roving inertial shaker method approach. Journal of Low Frequency Noise, Vibration and Active Control. https://doi.org/10.1177/14613484211039323
19. Peeters B, Van der Auweraer H, Guillaume P, Leuridan J (2004) The PolyMAX frequency-domain method: A new standard for modal parameter estimation? Shock Vib. https://doi.org/10.1155/2004/523692
20. Whalen TJ, Schöneich AG, Laurence SJ, Sullivan BT, Bodony DJ, Freydin M, Dowell EH, Buck GM (2020) Hypersonic fluid–structure interactions in compression corner shock-wave/boundary-layer interaction. AIAA J. https://doi.org/10.2514/1.J059152
21. Yu L, Pan B (2017) Single-camera high-speed stereo-digital image correlation for full-field vibration measurement. Mech Syst Signal Process. https://doi.org/10.1016/j.ymssp.2017.03.008
22. Yu L, Pan B (2018) High-speed stereo-digital image correlation using a single color high-speed camera. Appl Opt. https://doi.org/10.1364/AO.57.009257
23. Xie R, Yu L, Zhu W, Pan B (2020) Experimental study on flow-induced full-field vibration of a flexible splitter plate behind a cylinder using stereo-digital image correlation. J Vib Acoust. https://doi.org/10.1115/1.4048390
24. Witt BL, Rohe DP (2021) Digital image correlation as an experimental modal analysis capability. Exp Tech. https://doi.org/10.1007/s40799-020-00420-6
25. Frankovský P, Delyová I, Sivák P, Bocko J, Živčák J, Kicko M (2022) Modal analysis using digital image correlation technique. Materials. https://doi.org/10.3390/ma15165658
26. Jones EMC, Iadicola MA (Eds.) (2018) A good practices guide for digital image correlation. Int Digit Image Correl Soc. https://doi.org/10.32720/idics/gpg.ed1